Redox Biology 40 (2021) 101863

Contents lists available at ScienceDirect

Redox Biology

journal homepage: www.elsevier.com/locate/redox

Research Paper

Long non-coding RNA Meg3 deficiency impairs glucose homeostasis and insulin signaling by inducing cellular senescence of hepatic endothelium in obesity

Xiao Cheng [a,1], Mohamed Sham Shihabudeen Haider Ali [a,1], Matthew Moran [a], Martonio Ponte Viana [a], Sarah L. Schlichte [b], Matthew C. Zimmerman [b,c], Oleh Khalimonchuk [a,c,d], Mark W. Feinberg [e], Xinghui Sun [a,d,f,*]

[a] Department of Biochemistry, University of Nebraska - Lincoln, Beadle Center, 1901 Vine St, Lincoln, NE, 68588, USA
[b] Department of Cellular and Integrative Physiology, University of Nebraska Medical Center, 985850 Nebraska Medical Center, Omaha, NE, 68198-5850, USA
[c] Nebraska Redox Biology Center, University of Nebraska - Lincoln, USA
[d] Nebraska Center for Integrated Biomolecular Communication, University of Nebraska - Lincoln, USA
[e] Cardiovascular Division, Department of Medicine, Brigham and Women's Hospital, Harvard Medical School, Boston, MA, USA
[f] Nebraska Center for the Prevention of Obesity Diseases Through Dietary Molecules, University of Nebraska - Lincoln, USA

ARTICLE INFO

Keywords:
Long noncoding RNAs
Cellular senescence
Obesity
Hepatic endothelium
Glucose homeostasis

ABSTRACT

Obesity-induced insulin resistance is a risk factor for diabetes and cardiovascular disease. However, the mechanisms underlying endothelial senescence in obesity, and how it impacts obesity-induced insulin resistance remain incompletely understood. In this study, transcriptome analysis revealed that the long non-coding RNA (lncRNA) Maternally expressed gene 3 (Meg3) is one of the top differentially expressed lncRNAs in the vascular endothelium in diet-induced obese mice. Meg3 knockdown induces cellular senescence of endothelial cells characterized by increased senescence-associated β–galactosidase activity, increased levels of endogenous superoxide, impaired mitochondrial structure and function, and impaired autophagy. Moreover, Meg3 knockdown causes cellular senescence of hepatic endothelium in diet-induced obese mice. Furthermore, Meg3 expression is elevated in human nonalcoholic fatty livers and nonalcoholic steatohepatitis livers, which positively correlates with the expression of *CDKN2A* encoding p16, an important hallmark of cellular senescence. Meg3 knockdown potentiates obesity-induced insulin resistance and impairs glucose homeostasis. Insulin signaling is reduced by Meg3 knockdown in the liver and, to a lesser extent, in the skeletal muscle, but not in the visceral fat of obese mice. We found that the attenuation of cellular senescence of hepatic endothelium by ablating p53 expression in vascular endothelium can restore impaired glucose homeostasis and insulin signaling in obesity. In conclusion, our data demonstrate that cellular senescence of hepatic endothelium promotes obesity-induced insulin resistance, which is tightly regulated by the expression of Meg3. Our results suggest that manipulation of Meg3 expression may represent a novel approach to managing obesity-associated hepatic endothelial senescence and insulin resistance.

1. Introduction

Cellular senescence is a stable form of cell cycle arrest that can be induced by various stressors. Senescent cells display a number of hallmarks, including DNA damage, mitochondrial dysfunction, and increased cyclin-dependent kinase inhibitors and senescence-associated β-galactosidase (SA-β-gal) activity [1–4]. It is increasingly recognized that cellular senescence is heterogeneous and cell-specific with pleiotropic function [1,5–7]. Senescent cells are required for tissue remodeling and morphogenesis during embryonic development [8,9], are essential for wound healing [10], and promote heart regeneration after injury [11,12]. In contrast, targeted elimination of senescent cells prevents neurodegeneration [13], extends healthy life [14], and prevents Type 1 diabetes [15]. Recently, it was demonstrated that elimination of senescent cells improved glucose tolerance, enhanced insulin sensitivity,

* Corresponding author. Department of Biochemistry, Beadle N158, University of Nebraska – Lincoln, 1901 Vine Street, Lincoln, NE, 68588-0665, USA.
E-mail address: xsun17@unl.edu (X. Sun).
[1] X.C. and M.S.S. contributed equally to this work.

https://doi.org/10.1016/j.redox.2021.101863
Received 17 November 2020; Received in revised form 28 December 2020; Accepted 10 January 2021
Available online 19 January 2021
2213-2317/© 2021 The Authors. Published by Elsevier B.V. This is an open access article under the CC BY-NC-ND license (http://creativecommons.org/licenses/by-nc-nd/4.0/).

Abbreviations

CDKN1A	cyclin-dependent kinase inhibitor 1A
CDKN2A	cyclin-dependent kinase inhibitor 2A
ECs	endothelial cells
eWATs	epididymal white adipose tissues
GTTs	glucose tolerance tests
HFD	high-fat diet
HUVECs	human umbilical vein cells
IRβ	insulin receptor β
ITTs	insulin tolerance tests
LC3	microtubule associated protein 1 light chain 3
LncRNAs	long non-coding RNAs
Meg3	maternally expressed gene 3
NAFLD	nonalcoholic fatty liver disease
NASH	nonalcoholic steatohepatitis
OCR	O2 consumption rate
SA-β-gal	senescence-associated β-galactosidase

reduced macrophage accumulation in adipose tissue, lowered circulating inflammatory mediators, and promoted adipogenesis in obese mice [16]. These results indicate that cellular senescence is a causal factor in obesity-related inflammation and metabolic derangements. However, the role of senescent endothelial cells (ECs) in regulating the induction and exacerbation of obesity-induced insulin resistance is largely unknown [17].

Long non-coding RNAs (lncRNAs) are a subgroup of non-protein coding RNA transcripts that regulate gene expression in a range of signaling pathways, and changes in their expression and function contribute to the pathogenesis of human diseases [18–20] Emerging studies have shown that they are important regulators of cell stress responses [19–22]. We found that lncRNA Maternally expressed gene 3 (Meg3) protects endothelial function by regulating the DNA damage response [23]. In the present study, we identified Meg3 as a top differentially expressed lncRNA in the vascular endothelium of obese mice, and examined the role of Meg3 in regulating obesity-induced endothelial senescence and insulin resistance. We found that the loss of Meg3 induced hepatic endothelial senescence, and impaired glucose homeostasis and insulin signaling in obese mice. Meg3 knockdown induced cellular senescence by impeding mitochondrial function, facilitating the formation of mitochondria-derived reactive oxygen species, and impairing autophagy. Our findings demonstrate that hepatic endothelial senescence promotes obesity-induced insulin resistance.

2. Materials and methods

2.1. Mice

All methods reported herein were carried out in accordance with relevant guidelines and regulations of the University of Nebraska – Lincoln (UNL). All experimental protocols were reviewed and approved by UNL Institutional Biosafety Committee (Protocol Number: IBC788). Mouse experiments were performed in accordance with Public Health Service (PHS) animal welfare policy, the principles of the NIH Guide for the Care and Use of Laboratory Animals, and the policies and procedures at UNL. All animals were maintained in the UNL's centralized Life Sciences Annex facility, which is accredited by the Association for Assessment and Accreditation of Laboratory Animal Care. Mouse experiments were performed under Institutional Animal Care and Use Committee (IACUC) Protocol# 1820 (breeding) and Protocol# 1819 (experiments).

C57BL/6J mice were ordered from the Jackson Laboratory (stock #000664). The p53 floxed mice (Jackson stock #008462; $p53^{fl/fl}$) were bred with *Cdh5CreERT2* Cre mice [24,25] for two or three rounds to generate $p53^{fl/fl}$-Cre mice (p53 iECKO). A mouse model of diet-induced obesity was used in our studies. It has been widely used to dissect molecular mechanisms in obesity and obesity-impaired insulin signaling [26–31]. To examine Meg3 expression in lean and obese mice, two groups of C57BL/6J mice were used: one group was fed a high-fat diet (HFD; Research Diets D12492, 60% calories from fat) at 7 weeks of age for 4 or 8 weeks, and the second group was fed a control diet for D12492 (Research Diets D12450J, 10% calories from fat, matching sucrose and protein to D12492). To examine the effects of Meg3 on cellular senescence and glucose homeostasis, C57BL/6J mice or other mouse lines (see below) were fed a HFD (60% calories from fat, Research Diets D12492) at 7 weeks of age for 12 weeks. The p53 floxed mice or p53 iECKO mice were injected daily with tamoxifen (Sigma T5648; intraperitoneal 50 mg/kg) in corn oil for 5 days at 3–4 weeks of age as described [32]. Immediately after the last tamoxifen injection, $p53^{fl/fl}$ or p53 iECKO mice were fed a 60% HFD for 12 weeks. At Week 5 on HFD, C57BL/6J, $p53^{fl/fl}$, or p53 iECKO mice were randomly assigned into two groups and injected weekly with either negative control gapmeRs or Meg3 gapmeRs (intravenous 5 or 10 mg/kg) for 5 or 6 weeks. *In vivo* ready mouse Meg3 gapmeR (5′-TCATCAGTCAGTAGGT-3′) and LNA antisense negative control A (5′-AACACGTCTATACGC -3′) were purchased from Qiagen. To examine the effects of Meg3 knockdown on insulin signaling cascade *in vivo*, the mice were injected with insulin (0.75 U/kg Humulin R) after overnight fasting. The tissues were collected at 10 min after insulin injection.

2.2. Human liver specimens

Gene expression in human liver specimens was performed under the Institutional Review Board (IRB) Approval #: 20190419315EX. Normal human liver and pathologic human liver were obtained through the Liver Tissue Cell Distribution System, Minneapolis, MN.

2.3. Glucose tolerance and insulin tolerance tests

Glucose tolerance tests (GTTs) and insulin tolerance tests (ITTs) were performed as described in our previous studies [33]. For GTTs, mice were fasted for 12 h, and then injected with D-glucose (intraperitoneal 1.0 g per kg of body weight). ITTs were performed on mice after 6 h of fasting. Insulin (0.75 U/kg Humulin R) were given to mice by intraperitoneal injection. Blood glucose levels were measured before injection and at 15, 30, 60, 90, and 120 min after glucose or insulin injection using One Touch Ultra glucometer.

2.4. Cell culture

Human Umbilical Vein Cells (HUVECs) (cc-2159) were obtained from Lonza Group Ltd. and cultured in EC growth medium EGM-2 (cc-3162). Cells used for all experiments were subcultured <8 times. HUVECs (90,000/well) were plated into 12-well plates, transfected with 10 nM gapmeRs (LNA-modified antisense oligonucleotides) when cells reached 80–90% confluency. Lipofectamine 2000 (Thermo Fisher Cat# 11668019) was used following the manufacturer instructions. Human Meg3 gapmeR (5′-GTAAGACAAGCAAGAG-3′), and LNA antisense negative control A (5′-AACACGTCTATACGC -3′) were purchased from Qiagen.

For western blot analysis of p62 and LC3 II, HUVECs were treated with 100 nM Bafilomycin A1 (Sigma Cat# B1793) for 4 h. For SA-β-gal staining, cells were treated with 20 nM rapamycin (Sigma Cat# R8781) for 48 h.

2.5. Endothelial cell isolation

For the sample preparation for RNA-seq, C57BL/6J mice were ordered from the Jackson Laboratory (stock #000664). Mice were fed on a high-fat diet (60% calories from fat, Research Diets D12492) at 8 weeks

of age for 5 weeks (6 mice; n = 2 mice each sample). Mice fed on a regular chow diet were used as controls (9 mice; n = 3 mice each sample). For other experiments, mice were fed on a 60% HFD or treated as indicated before EC isolation. The method for isolation of mouse ECs was modified from previous studies [33–36]. Mice were euthanized by 30% isoflurane. Livers, eWATs, or skeletal muscles were harvested, washed with 1 x dPBS to remove any contaminants. Tissues were minced into small pieces with scissors followed by digestion with 10 ml digestion buffer (collagenase type 2, Worthington-Biochem, Cat# LS004177, 1mg/ml in DMEM/F12; dipase II, Roche, Cat# 04942078001, 1 mg/ml in DMEM/F12) for 40 min in a 37 °C shaker. Cell slurry was transferred onto a 100 μm cell strainer pre-wet with equal volume of wash medium (DMEM/F12 medium with 10%FBS), then span at 500×*g* for 10 min. Supernatant was gently aspirated and discarded, and cell pellet was re-suspended in 10 ml wash medium followed by second filtering with 40 μm cell strainer and spinning at 500×*g* for 10 min. Supernatant was gently aspirated and cell pellet was mixed with 1 ml incubation buffer (0.1% BSA, 2 mM EDTA and 0.5% FBS in 1 x dPBS). Cell suspension was incubated with sheep anti-rat IgG Dynabeads (Thermo Fisher, Cat# 11035) coated with PECAM-1 antibodies (Becton Dickinson Co, Cat# 557355) and tumbled at 4 °C for 15 min. After incubation, beads were separated by using magnetic separation rack (NEB, Cat# S1509S), and washed with 1 ml of 0.1% BSA in PBS twice, then mixed with 500 μl TRIzol reagent for each sample followed by RNA extraction according to the manufacturer's instructions.

2.6. Senescence-associated β-gal staining

HUVECs were seeded into two T25 flasks (750,000 cells/flask), and transfected with 10 nM negative control or Meg3 gapmeRs using Lipofectamine 2000 on the next day. After 16 h, medium was replaced and changed every two days. On day 5 after transfection, cells were plated to 12-well plate (90,000 cells/well). For double knockdown of p53 and Meg3, HUVECs (750,000 cells/flask) were seeded into two T25 flasks. Cells were transduced by lentiviral control shRNA or p53 shRNA generated as described in our previous studies [23]. After 24 h, cells were split to two flasks. On the next day, cells were transfected with negative control or Meg3 gapmeRs using Lipofectamine 2000. Medium were changed at 16 h post-transfection and cells were plated into 12-well plate (90,000 cells/well) at 72 h after transfection. β-galactosidase staining was performed using Senescence β-galactosidase Staining Kit according to the manufacturer's instructions (Cell Signaling Technology, #9860) at 96 h post-transfection.

2.7. MitoSOX staining

To measure mitochondrial superoxide production, HUVECs were stained with MitoSOX™ Red superoxide radical-specific reagent as described [37–39]. HUVECs were incubated with 1 μM MitoSOX dye (Thermo Fisher, Cat# M36008) in 1 x HBSS with Ca^{2+} and Mg^{2+} for 10 min, washed three times with 1 x HBSS with Ca^{2+} and Mg^{2+}. Cells were trypsinized and re-suspended in 1 x HBSS buffer with Ca^{2+} and Mg^{2+} for flow cytometry analysis immediately [40,41]. MitoSOX was excited with 488 nm laser, and Texas red filter (610/40 nm) was used to detect the emission by flow cytometry.

2.8. Electron paramagnetic resonance (EPR) spectroscopy

HUVECs were transfected with 10 nM control gapmeRs or Meg3 gapmeRs. 40 h post-transfection, cells were collected for EPR as described previously [42,43]. After removing cell culture media, cells were incubated in 1 mL of Krebs-HEPES Buffer (pH 7.4) containing (in mM): 99 NaCl, 4.69 KCl, 2.5 $CaCl_2$, 1.2 $MgSO_4$, 25 $NaHCO_3$, 1.03 KH_2PO_4, 5.6 D-glucose, 20 HEPES, and supplemented with the metal chelators deferoxamine (25 μM) and diethyldithiocarbamic acid sodium salt (5 μM). The superoxide-sensitive EPR spin probe, 1-hydroxy-3-methoxycarbonyl-2, 2, 5, 5-tetramethylpyrrolidine (CMH) was added to get 200 μM final concentration, and incubated for 30 min at 37 °C. Then, 900 μl of buffer was removed and cells were collected by scraping in the remaining 100 μl. The sample (50 μl) was then loaded into a glass capillary tube and inserted into the capillary holder of a Bruker e-scan EPR spectrometer. The following EPR spectrometer settings were used: field sweep width, 60.0 G; microwave frequency, 9.74 kHz; microwave power, 21.90 mW; modulation amplitude, 2.37 G; conversion time, 10.24 ms; time constant, 40.96 ms. The EPR spectrum amplitude, which is directly proportional to the levels of free radicals in the sample, was normalized to cell number in each sample.

2.9. Assessment of mitochondrial bioenergetics

To measure mitochondrial respiration, transfected HUVECs were plated in 24-well Seahorse culture plates (95% confluency, 20,000 cells/well) one day prior to measurement. For O_2 consumption rate (OCR) measurement, cell culture media were changed to modified XF assay medium containing 10 mM glucose, 1 mM sodium pyruvate and 2 mM L-glutamine. Following 1 h incubation at 37 °C without CO_2, OCR were measured using Seahorse XFe24 extracellular flux analyzer according to manufacturer's instruction in response to the respiratory chain inhibitors: 1 μM Oligomycin, 1 μM FCCP, 1.5 μM antimycin A and 3 μM rotenone.

2.10. RNA sequencing and analysis

Total RNAs were extracted from the isolated ECs using TRIzol reagent (ThermoFisher, Cat# 15596018) according to the manufacturer's instructions. RNA samples were in triplicates. RNA-seq analysis was performed by Genewiz (Formerly Beckman Coulter Genomics). Ribosomal RNAs were depleted using TruSeq Stranded Total RNA with Ribo-Zero Gold kit. Then, stranded RNA-seq automated libraries were constructed for sequencing on an Illumina HiSeq 2500 (2 x 100 bp). After obtaining raw reads, FastQC was used to analyze the quality of the reads. The number of quality control-passed reads is at least 45 million per sample. Tophat2 and bowtie [44–46] were used to map the reads to the genome, GRCh38, Ensembl release 82 [47], and cufflinks [48] was used to determine transcript expression. Cuffdiff [49] was used to generate FPKM values and edgeR [50–53] was used for differential expression analysis. Heatmap was generated using the R pheatmap package, and genes were ranked on logFC of FPKMs.

2.11. Immunofluorescence and imaging

Tissues were fixed in 10% formalin (Sigma, Cat# HT5012-60 ML) for 24 h at 4 °C. The fixed tissues were immersed in 10% sucrose for 2 days and subsequently in 30% sucrose for 2 days. Then the tissues were embedded in cryomolds with optimal cutting temperature compound (Fisher Scientific, Cat# 4585) and allowed to freeze on dry ice. Frozen tissues were sectioned using cryostat microtome and the sections were mounted on poly-lysine coated slides (Thermo Fisher, Cat# P4981-001). The slides with mounted tissue sections were immersed in 1:1 solution of acetone:methanol mixture at 4 °C for 10 min and then washed with 1 x dPBS containing 0.3% Triton X-100 (PBST) three times with 5 min for each. The sections were then blocked with 0.3% PBST containing 5% goat serum and 1% BSA. Primary antibodies at dilutions, 1:100 for p21 (Abcam, Cat# Ab188224), 1:100 for CD31 (BD, Cat# 550274), 1:500 for CD68 (BioLegend, Cat#137001), 1:2000 for Mac-2 (Cedarlane, Cat# CL8942AP), 1:500 for perilipin (Cell Signaling Technology, Cat# 9349S) were used for overnight staining at 4 °C. Slides were washed three times with 0.3% PBST for 5 min each. Subsequently, the slides were incubated with appropriate secondary antibodies at dilution, 1: 200 for DyLight® 549 anti-Mouse IgG (Vector, Cat# DI-2549); 1:200 for DyLight® 649 anti-Rabbit IgG (Vector, Cat# DI-1649); 1:200 for Cy™3 AffiniPure goat anti-Rat IgG (H + L) (Jackson Immunoresearch, Cat# 112-165-167)

with DAPI for nuclear staining for 1 h at room temperature. After the slides were washed three times with 0.3% PBST, 5 min each, they were mounted with coverslips using Fluoromount-G® (Southern biotech, Cat# 0100–01) and allowed to dry overnight in dark at room temperature. Images were captured using Fluorescent microscope. Three random fields per tissue sample were captured and the images were analyzed for appropriate staining.

2.12. Quantitative real-time PCR (qPCR)

RNA was collected from HUVECs or mouse tissues using TRIzol Reagent (Thermo Fisher, Cat# 15596026) according to the manufacturer's instructions. 1 μg of RNA was converted to cDNAs using the High Capacity cDNA Reverse Transcription Kit (Thermo Fisher, Cat# 4368814). qPCRs were conducted in the CFX Connect Real Time System (BioRad) using 2x SYBR Green qPCR Master Mix (Bimake, Cat# B21203). Data was normalized by the ΔΔCt method [54]. Primer sequences are listed in the Supplementary Table 1.

2.13. Western blot analysis

Mouse tissues were homogenized in RIPA buffer (25 mM Tris-HCl pH 7.6, 150 mM NaCl, 1% NP-40, 1% sodium deoxycholate, 0.1% SDS) that was supplemented with protease and phosphatase inhibitors. Cell lysates were collected after spinning at 13,000×*g* for 10 min. Protein concentrations were measured by using the Pierce BCA Protein Assay Kit (Thermo Fisher). 10 μg of protein was loaded per sample and the samples were separated by SDS-PAGE using a 10% or 12% acrylamide gel. After SDS-PAGE, the samples were transferred to Immun-Blot PVDF Membranes using the Trans Blot Turbo Transfer System (BioRad; 25 V, 1.0 A, 30 min). After blocking with 5% nonfat milk in TBST, membranes were incubated with corresponding antibodies. Then the blot was probed with HRP-conjugated anti-rabbit (Cell Signaling Technology, Cat# 7074). ECL Plus Western blotting detection reagents (GE Healthcare, Cat# RPN2132) were used to visualize proteins. ImageJ software (National Institutes of Health) was used to analyze protein abundance. Antibodies used in this study include anti-Phospho-Akt (Ser473) (Cell Signaling Technology, Cat# 4060S), anti-Akt (Cell Signaling Technology, Cat# 4691S), anti-p62 (MBL international, Cat# PM045), anti-LC3B (Cell Signaling Technology, Cat# 3868S), anti-Phospho-IGF-I Receptor β (Tyr1135/1136)/Insulin Receptor β (Tyr1150/1151) (Cell Signaling Technology, Cat# 3024S), anti-Insulin Receptor β (Cell Signaling Technology, Cat# 3025S), anti-p53 (Cell Signaling Technology, Cat# 9282S), and anti-GAPDH (Cell Signaling Technology, Cat# 5174). Protease inhibitor cocktail tablets were from Roche Diagnostics. Phosphatase inhibitor was from Active Motif.

2.14. Live cell imaging

Live cell imaging was carried out using a Nikon A1R-TiE (inverted) confocal live-cell imaging system. An incubation chamber was used to maintain the live cell conditions (5% CO_2 and 37 °C with humidity). Cells cultured in a 35 mm glass bottom dish were used for imaging using 100x (NA 1.4) oil immersion lens with the help of NIS elements software by sequential scanning, where applicable. For mitochondrial network staining, cells were incubated with 300 nM MitoTracker Deep Red dye at 37 °C for 10 min in 1 x HBSS with calcium and magnesium and washed twice before imaging. Cells were excited by 640 nm laser and emissions were collected at 640–690 nm range. HUVECs were also stained with 500 nM MitoTracker Green for 30 min and treated with 10 μM FCCP for 10 min for live cell imaging. For membrane potential staining, cells were stained with 5 μg/ml JC-1 dye at 37 °C for 15 min in 1 x HBSS with calcium and magnesium and washed twice. JC1 was excited by the 488 nm and 561 nm lasers, and emissions were collected between 500 - 550 nm and 570–620 nm. Nuclei stained with Hoechst was excited at 405 nm wavelength laser and emission was collected between 425 and 475 nm. Mitochondrial structure was analyzed using a custom-modified NIH ImageJ macro [55,56]. Form factor = Perimeter^2/(4 × Pi × area). Mitochondrial perimeter is defined as the number of pixels forming the boundary of a mitochondrial region.

2.15. ELISA

Plasma levels of insulin, adiponectin, TNF-α, MCP-1 were measured by Eve Technologies Corp., and plasma levels of AST and ALT were measured by the Biomedical and Obesity Research Core at UNL.

2.16. Statistical analysis

For two-group comparisons, paired or unpaired Student's t-test was used for data that passed normality and equal variance test; otherwise, a nonparametric Mann-Whitney *U* test will be used. For multiple groups, one-way ANOVA followed by Tukey's post hoc test was used for data that passed normality and equal variance test; otherwise one-way ANOVA followed by Holm's post hoc test will be used. Normality will be checked with the Kolmogorov-Smirnov test. An alpha level of 0.05 were used to determine significant differences, and data are reported as mean ± SEM.

3. Results

3.1. Endothelial Meg3 expression is elevated in obesity

To identify differentially expressed lncRNAs in vascular endothelium in obese mice, the ECs of epididymal white adipose tissues (eWATs) were isolated from lean and obese mice for global transcriptomic analysis using RNA-seq (Fig. 1A). The bioinformatics analysis identified 34 differentially expressed lncRNAs using edgeR (Fig. 1B). Among these lncRNA transcripts, Meg3 is one of the top induced lncRNAs (Fig. 1B). We examined Meg3 expression in the vascular endothelium of major insulin target organs in lean and obese mice. After 4 weeks of high-fat diet (HFD), Meg3 expression was induced by 1.6-, 1.5-, and 1.7-fold in ECs isolated from eWATs, skeletal muscles, and livers of obese mice, respectively; after 8 weeks of HFD, Meg3 expression was induced by 2.0-, 1.9-, and 2.3-fold, respectively (Fig. 1C). Meg3 expression is higher in the ECs from eWAT compared to those from the skeletal muscle or liver (Fig. 1D). Meg3 *in situ* hybridization revealed that the majority of Meg3 is expressed in the nucleus of mouse and human adipose tissues co-localizing with the nuclei of adjacent CD31 positive cells (Fig. S1). These data demonstrate that Meg3 is induced in the vascular endothelium of diet-induced obese mice.

3.2. Meg3 knockdown causes cellular senescence in HUVECs

Meg3 expression is elevated in senescent HUVECs compared with early passage cells [57], and in HUVECs exposed to oxidative stress [58] and hypoxia [59]. We have shown that DNA damaging agents induced Meg3 expression in HUVECs in a p53-dependent manner, and Meg3 knockdown induced DNA damage and inhibited EC proliferation [23]. Meg3 knockdown also reduced the telomere length in HUVECs [60]. However, the role of Meg3 in cellular senescence has not been thoroughly investigated.

Here, we studied the effects of Meg3 on cellular senescence by examining several complementary hallmarks of cellular senescence in HUVECs, including SA-β-gal activity, mitochondrial dysfunction, and autophagy (Fig. 2). SA-β-gal activity is one of the commonly used marker for senescence *in vitro* and *in vivo* [61,62]. We found that Meg3 knockdown increased the levels of SA-β-gal activity by 2.7-fold (Fig. 2A). Mitochondrial dysfunction and mitochondria-derived superoxide are key hallmarks of cellular senescence [63–66]. We asked whether Meg3 knockdown increases levels of superoxide in HUVECs. Superoxide-specific MitoSOX staining and flow cytometry revealed that

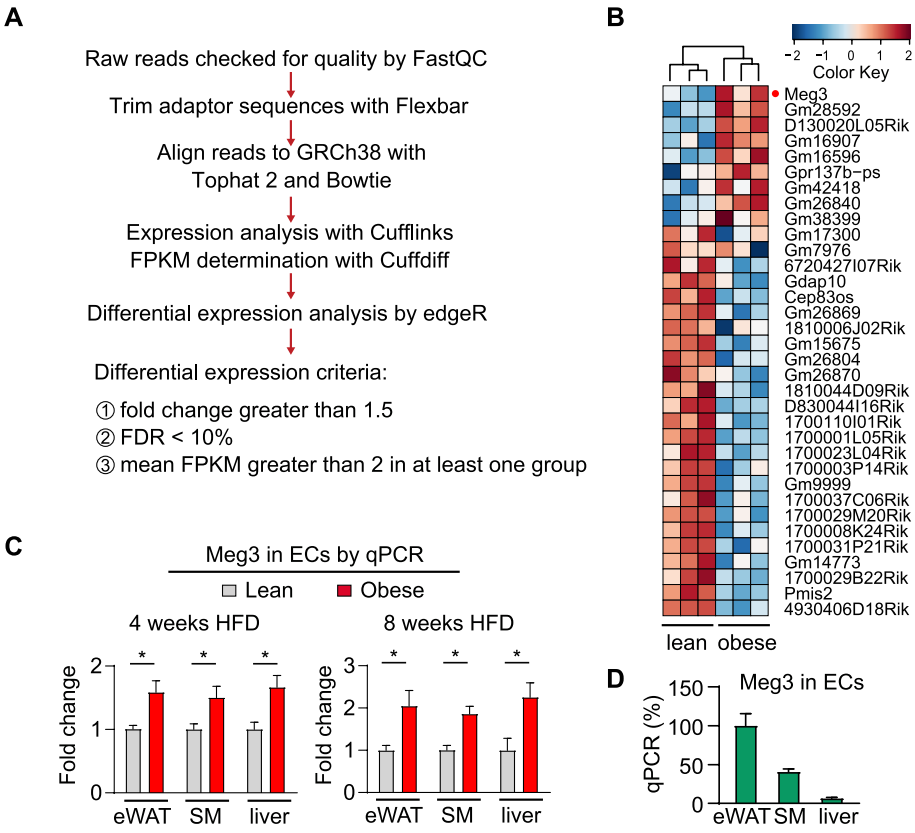

Fig. 1. LncRNA Meg3 expression is induced in vascular endothelium of obese mice. (A) Workflow of genome-wide RNA-seq profiling for the identification of differentially expressed lncRNAs (fold change >1.5; FDR<0.1; mean FPKM greater than 2 in at least one group). (B) Heatmap displaying significantly dysregulated lncRNAs identified by edgeR. (C) Meg3 expression was detected in the ECs isolated from the eWATs, livers, or skeletal muscles (SM) of lean or obese mice by qPCR. Mice were fed a control diet or high-fat diet (HFD) for 4 weeks (n = 7–10 for lean and n = 9–12 for obese) or 8 weeks (n = 8 for lean and n = 8 for obese). (D) Meg3 expression was compared among ECs from eWATs, livers, and skeletal muscles. The expression of Meg3 in eWATs was set as 100 (n = 15 mice). For all panels, values are mean ± SEM; *, $P < 0.05$.

HUVECs with Meg3 knockdown showed a marked increase in superoxide (Fig. 2B). Free radicals, primarily superoxide, were measured by Electron Paramagnetic Resonance (EPR) Spectroscopy [42,43]. Consistent with the MitoSOX staining data, HUVECs with Meg3 knockdown displayed a significant increase in superoxide levels compared to control cells (Fig. 2C), as indicated by an increase in the EPR spectrum amplitude. We examined the effects of Meg3 knockdown on mitochondrial bioenergetic function in HUVECs including mitochondrial respiration and cellular glycolysis. Meg3 knockdown reduced the basal mitochondrial O_2 consumption rate and the maximal respiration capacity (Fig. 2D). Meg3 knockdown did not affect the extracellular acidification rate, which is a proxy to cellular glycolytic flux (Fig. S2). We next sought to determine the effect of Meg3 knockdown on mitochondrial morphology using a custom-modified NIH Image J macro [55,56]. We found that mitochondria were predominantly fragmented in HUVECs with Meg3 knockdown (Fig. 2E), which is comparable with the effects of FCCP, a chemical uncoupler that potently induces mitochondrial fragmentation (Fig. S3). These changes in mitochondrial network are associated with the attenuated mitochondrial membrane potential in HUVECs with Meg3 knockdown (Fig. 2F). These data demonstrate that Meg3 knockdown impairs mitochondrial structure and function. Finally, we examined the effects of Meg3 knockdown on autophagy because impaired autophagy can promote cellular senescence in ECs [67,68]. The expression of both p62 and LC3-II were induced by Meg3 knockdown in HUVECs under basal condition (Fig. 2G). When cells were treated with Bafilomycin A1, both p62 and LC3-II accumulation were comparable between control cells and cells with Meg3 knockdown, though the expression of p62 showed a tendency towards statistical significance (Fig. 2G). Our data demonstrate that Meg3 knockdown alters autophagic flux likely by impairing autophagy in HUVECs. Moreover, the activation of autophagy by rapamycin attenuated Meg3 knockdown-induced SA-β-gal activity in HUVECs, suggesting that Meg3 knockdown promotes cellular senescence likely by impairing autophagy in HUVECs (Fig. 2H).

In summary, these data along with our published results showing that Meg3 knockdown induced DNA damage and inhibited cell proliferation [23] demonstrate that Meg3 prevents cellular senescence in HUVECs.

3.3. *Meg3 knockdown causes cellular senescence in hepatic endothelium in obesity*

Our data suggest that Meg3 is required to limit endothelial senescence *in vitro*. This prompted us to ask if Meg3 knockdown affects cellular senescence in mice. We used a mouse model of diet-induced obesity in our studies. In this model, mice develop obesity, elevated adiposity, glucose intolerance, moderate insulin resistance, and hyperinsulinemia compared with lean mice, which mimics human metabolic derangements observed in obesity [69–73]. We employed locked nucleic acid-modified antisense oligonucleotides (gapmeRs) that have been used for highly efficient inhibition of lncRNA function [59,74,75]. Meg3 knockdown by intravenous delivery of Meg3 gapmeRs induced the expression of p53 target genes *GADD45A* and *RRAD* by 2.4- and 1.7-fold, respectively, in ECs isolated from the livers (Fig. 3A). Meg3 knockdown also induced the expression of cyclin-dependent kinase inhibitors including two markers of senescence [76–78] *CDKN1A* (encoding p21) by 2.7-fold and *CDKN2A* (encoding p16) by 3.4-fold, in the ECs isolated from the livers of obese mice (Fig. 3A). In the ECs isolated from skeletal muscles, *GADD45A* is the only induced gene among these examined genes, and its expression was elevated by 1.7-fold (Fig. 3A). In the ECs isolated from the eWATs, *CDKN2A* is the only induced gene, and its expression was elevated by 2.0-fold (Fig. 3A). These changes in gene expression were associated with a 94.3%, 90.0%, and 75.2% reduction of Meg3 expression in the ECs isolated from the liver, skeletal muscle, and eWAT, respectively (Fig. 3B). The expression of p21 was also examined by immunostaining on frozen liver sections. Meg3 knockdown led to a 10.3-fold increase in the number of p21-positive cells that co-localize with CD31-positive cells in the livers of obese mice (Fig. 3C).

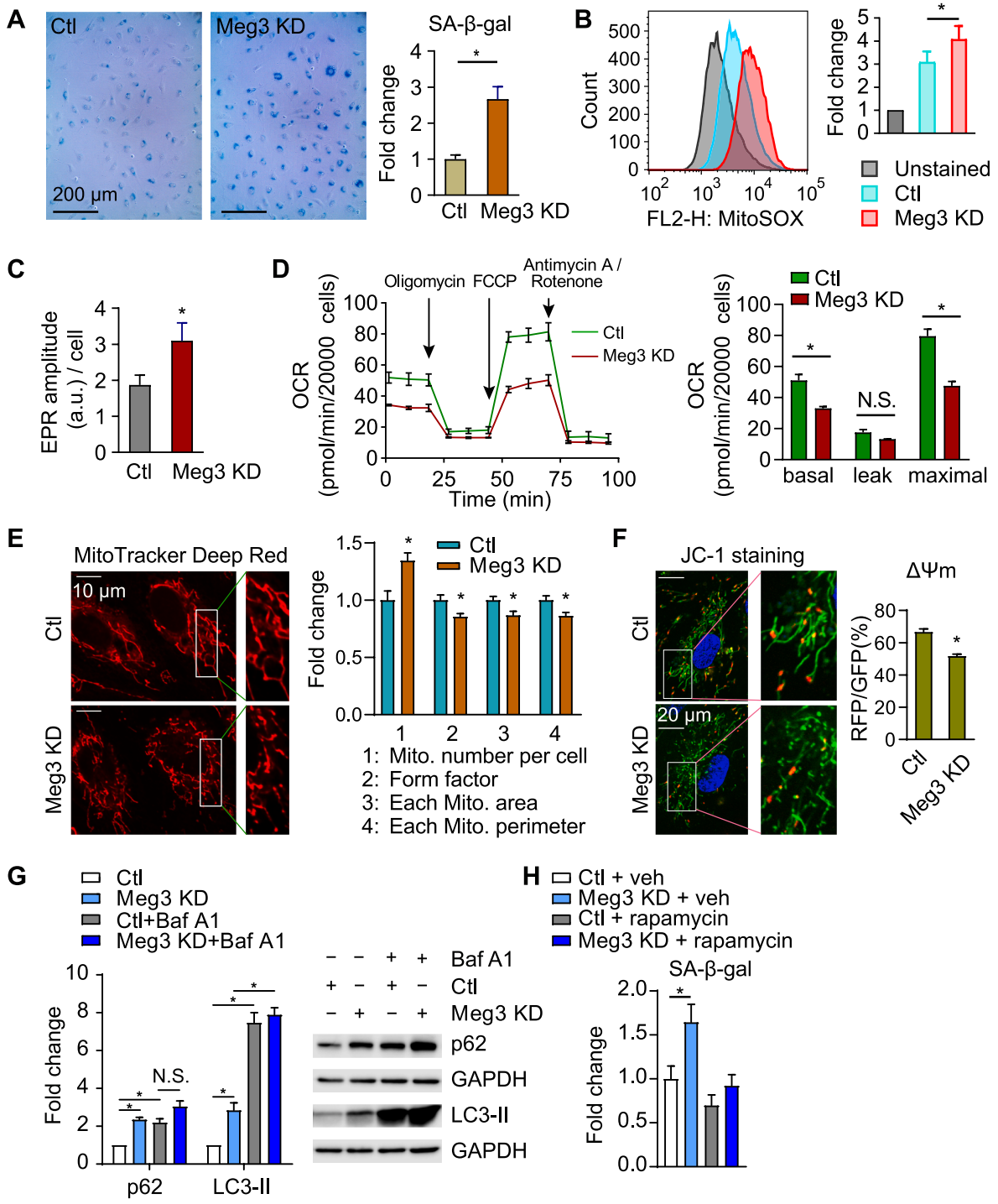

Fig. 2. Meg3 knockdown (KD) causes cellular senescence of HUVECs. HUVECs were transfected with 10 nM control gapmeRs or 10 nM Meg3 gapmeRs. (A) Fold change of SA-β-gal positive cells were calculated from 36 images per condition (n = 3). (B) MitoSOX reagent staining and flow cytometry analysis (n = 3). (C) Levels of endogenous free radicals, primarily superoxide, measured by electron paramagnetic resonance (EPR), with n = 10 or 11 replicates (n = 3). (D) Oxygen consumption rate (OCR) in HUVECs (n = 3). (E) Mitochondria revealed by mitoTracker deep red in live cells. 101 or 75 cells (n = 4) were analyzed. (F) Mitochondrial membrane potential (ΔΨm) revealed by JC-1 staining in live cells. Data from 32 or 40 cells (n = 3). (G) Western blot analysis of p62 and LC3-II in the presence or absence of bafilomycin A1 (Baf A1) (n = 3). N.S., non-significant. (H) Fold change of SA-β-gal positive cells were calculated from 30 images per condition in the presence or absence of rapamycin (n = 3). For all panels, values are mean ± SEM; n = 3 refers to three independent experiments; *, $P < 0.05$. (For interpretation of the references to colour in this figure legend, the reader is referred to the Web version of this article.)

In the liver, skeletal muscle, and eWAT tissues with a mixed cell populations, *CDKN2A* is the only gene induced by Meg3 knockdown among examined genes; its expression was induced by 2-fold in the liver but not in the skeletal muscle and eWAT (Fig. 3D). These data demonstrate that Meg3 knockdown promotes cellular senescence of hepatic endothelium with no or minimal effects on cellular senescence of other cell types in the liver, skeletal muscle, and eWAT.

We next examined Meg3 expression in human liver specimens provided by the Liver Tissue Cell Distribution System at the University of Minnesota. Demographics of these liver specimens are shown in

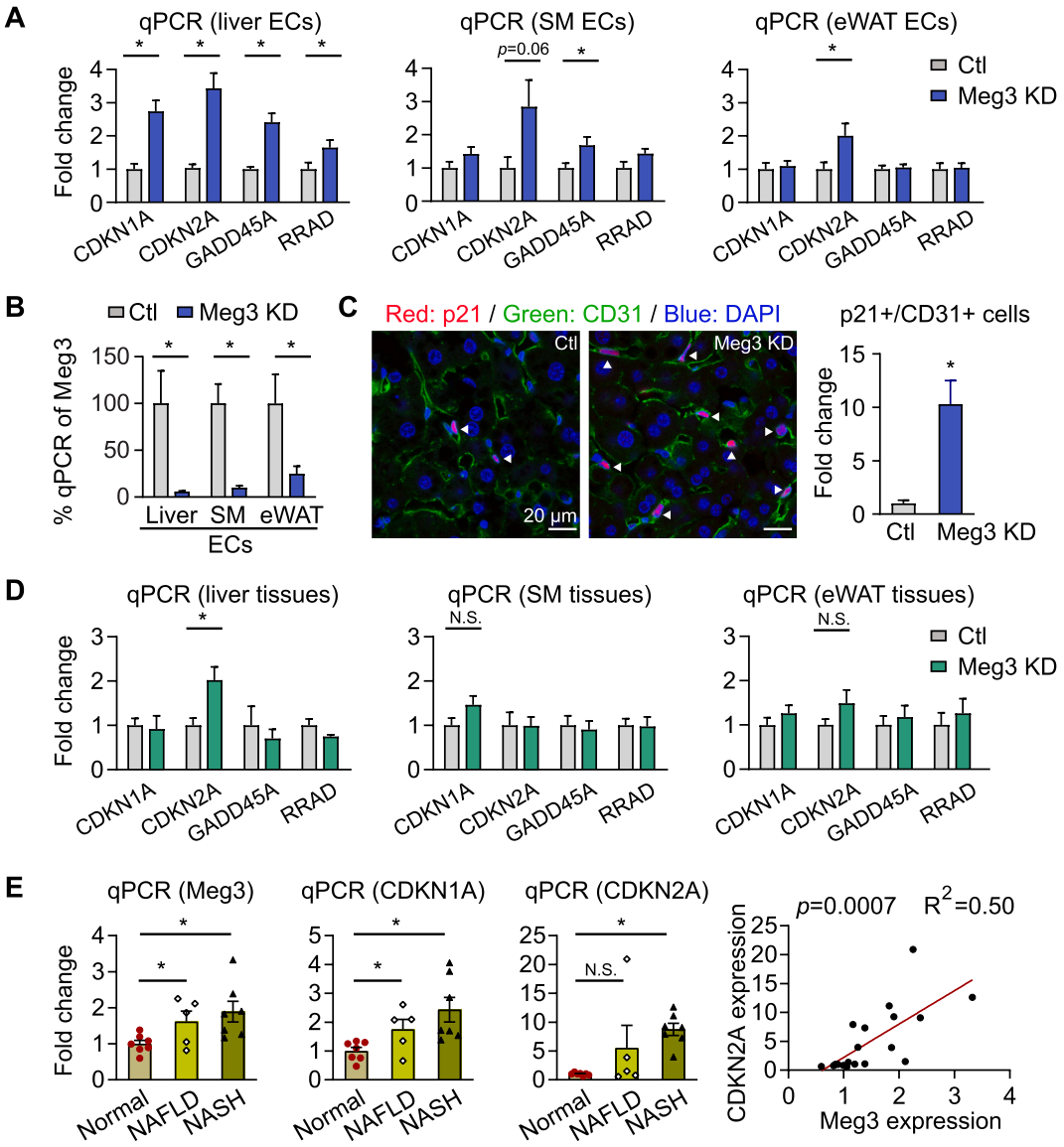

Fig. 3. Meg3 knockdown (KD) causes cellular senescence in hepatic vascular endothelium in obesity. (A–D) C57BL/6 mice were fed on a HFD and treated with control gapmeRs (n = 6) or Meg3 gapmeRs (n = 7) as described in Methods. (A) The expression of senescent markers (CDKN1A and CDKN2A) and p53 target genes (GADD45A and RRAD) were examined in the freshly isolated ECs of livers, skeletal muscles (SM), and eWATs by qPCR. (B) The expression of Meg3 were examined in isolated ECs by qPCR. (C) Immunofluorescence staining of liver sections with anti-CD31 and anti-p21 antibodies. The percentage of p21 positive cells was calculated among CD31 positive cells, which was set as 1 in mice injected with control gapmeRs. Several double positive cells are indicated by arrowheads. (D) The expression of senescent markers (CDKN1A and CDKN2A) and p53 target genes (GADD45A and RRAD) were examined in livers, skeletal muscles, and eWATs tissues by qPCR. (E) The expressions of Meg3, CDKN1A, and CDKN2A were analyzed in RNAs isolated from liver specimens of human subjects without fatty liver (n = 7), with nonalcohlic fatty liver (NAFLD; n = 5) or nonalcohlic hepatosteatosis (NASH, the severe form of fatty liver; n = 7). For all panels, values are mean ± SEM; *, $P < 0.05$.

Supplementary Table 2. Nonalcoholic steatohepatitis (NASH) is the more aggressive form of nonalcoholic fatty liver disease (NAFLD). Meg3 expression was elevated by 1.6- and 1.9-fold, respectively, in NAFLD and NASH livers (Fig. 3E). Furthermore, *CDKN1A* expression was 1.8-fold higher in NAFLD and 2.4-fold higher in NASH livers, respectively; and the expression of *CDKN2A* was 8.8-fold higher in NASH livers (Fig. 3E). Importantly, the expression of Meg3 positively correlates with *CDKN2A* expression in these human liver specimens (Fig. 3E).

Taken together, these data suggest endogenous Meg3 limits cell senescence of hepatic vascular endothelium in diet-induced obese mice and has translational relevance to human subjects, although additional features of cellular senescence such as impaired autophagy and mitochondrial structure and function were not examined in hepatic endothelium in the present study.

3.4. Meg3 knockdown impairs insulin signaling and glucose homeostasis

Senescent cells are found in obesity [78–81]. Because we found Meg3 knockdown promotes cellular senescence in hepatic endothelium in obesity, we next sought to examine the role of Meg3 in obesity-induced insulin resistance and glucose homeostasis. The intravenous delivery of Meg3 gapmeRs led to 94.8%, 89.8%, and 68.9% reduction of Meg3 expression in the liver, skeletal muscle, and eWAT, respectively (Fig. 4A). Meg3 knockdown did not affect food intake, body weight, physical activity, heat, carbon dioxide production, or oxygen consumption revealed by metabolic cage studies (Fig. S4). Glucose tolerance test (GTT) and insulin tolerance test (ITT) revealed that Meg3 gapmeR-treated mice developed more severe glucose intolerance and insulin resistance after being fed a HFD for 10 weeks (Fig. 4B and C). In addition, Meg3 gapmeRs-treated mice had higher fasting plasma insulin

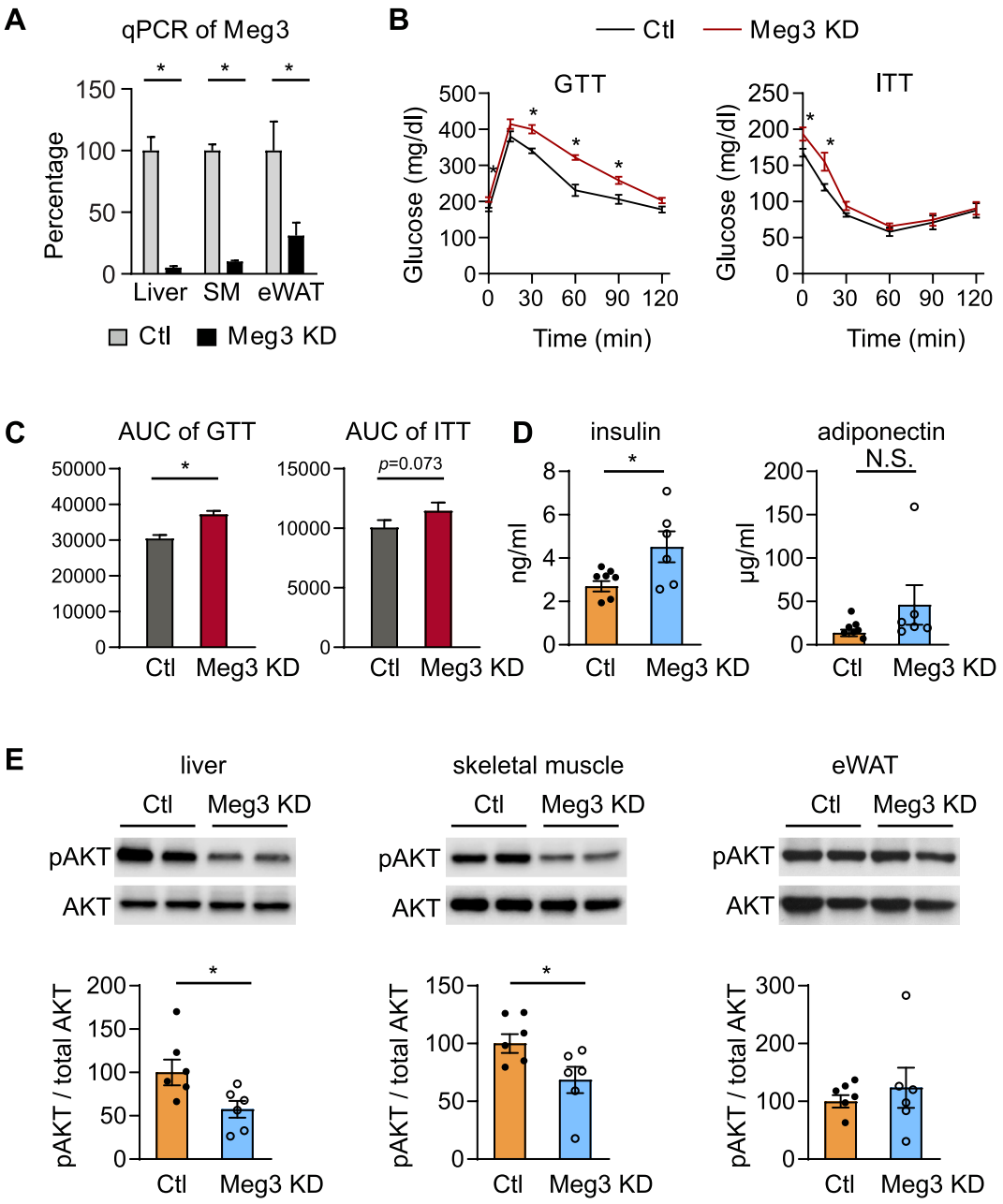

Fig. 4. Meg3 knockdown (KD) induces obesity-associated insulin resistance. C57BL/6 mice were fed a HFD. At Week 5 on HFD, mice were intravenously injected with control gapmeRs or Meg3 gapmeRs once a week and maintained on HFD up to 12 weeks. (A) Meg3 expression was examined in livers, skeletal muscles, and eWATs tissues by qPCR. (B) Glucose and insulin tolerance tests. (C) Areas under curves (AUC) for GTT and ITT. (D) The fasting levels of plasma insulin and adiponectin were examined by ELISA. A small amount of blood were collected before insulin injection. (E) Total Akt and the phosphorylation of Akt at serine 473 were examined by western blot in the indicated tissues of overnight-fasted mice. The tissues were collected at 10 min after insulin injection (0.75 units/kg). For all panels, values are mean ± SEM, n = 6–7; *, $P < 0.05$.

levels but not adiponectin (Fig. 4D). To ensure these findings are linked to changes in insulin signaling, we examined Akt phosphorylation at serine 473 (pSer473-Akt) in the liver, skeletal muscle, and eWAT of obese mice injected with insulin. Meg3 knockdown reduced the levels of pSer473-Akt by 43% in the livers and by 32% in the skeletal muscles but not in the eWATs in obese mice (Fig. 4E). We also examined the effects of Meg3 knockdown on the levels of phosphorylated insulin receptor β subunit (IRβ), a key upstream component of insulin signaling cascade. Meg3 knockdown reduced the levels of phosphorylated IRβ by 50% in the livers of obese mice (Fig. S5). These data demonstrate that Meg3 knockdown impairs systemic glucose homeostasis and insulin sensitivity in the liver and skeletal muscle.

Chronic inflammation is a key driver of obesity-induced insulin resistance [82–84]. Histological assessment of eWAT by macrophage marker Mac2 revealed no differences between two groups of obese mice injected with negative control or Meg3 gapmeRs (Fig. S6A). The expression of TNF-α and ICAM-1 was unaltered at the mRNA levels in eWAT (Fig. S6B). Interestingly, histological assessment of livers by CD68 staining revealed a 37% decrease in macrophage content in the HFD-fed mice injected with Meg3 gapmeRs compared to livers of the HFD-fed control mice (Fig. S6C). The mRNA expression of CD68 and F4/80 were also reduced, while the mRNA expression of MCP1 was unchanged (Fig. S6D). In addition, the plasma levels of TNF-α and MCP1 were not changed in mice with Meg3 knockdown (Fig. S6E), suggesting that Meg3

knockdown had no effects on systemic inflammation. Finally, the levels of plasma ALT and AST were not changed by Meg3 knockdown (Fig. S6F). But interestingly, Meg3 knockdown induced type I interferon response in hepatic endothelium as revealed by the induction of IFN-β and IRGM (immunity-related GTPase family M) expression at mRNA levels (Fig. S6G). Consistent with the data, Meg3 knockdown also induced type I interferon response in HUVECs (Fig. S6G). These data demonstrate that Meg3 knockdown-induced insulin resistance is unlikely to arise from its effects on systemic inflammation.

To interrogate the proteome regulated by Meg3 *in vivo*, livers were collected for quantitative proteomics analysis (Fig. S7). TMT10-plex labeling and mass spectrometry identified 104 differentially expressed proteins (20% change with $P < 0.05$) (Supplementary Table 3). Genes encoding these proteins were used for gene ontology (GO) term analysis. The top 10 GO terms by fold enrichment are shown in Fig. S7. The top three terms are "Mitochondrial respiratory chain complex I″, "Respiratory chain", and "Response to oxidative stress", indicating that Meg3 knockdown impairs mitochondrial function in liver of obese mice. These data suggest that Meg3 knockdown induces mitochondrial stress *in vivo*.

Taken together, these data demonstrate that Meg3 knockdown impairs systemic glucose homeostasis and insulin signaling in the liver and skeletal muscle independent of its any effects on systemic inflammation.

3.5. Endothelial cell-specific p53 knockout attenuates Meg3 knockdown-induced cellular senescence in hepatic endothelium

An important question that we wished to address is whether cellular senescence of the vascular endothelium impairs glucose homeostasis and insulin signaling in obesity. Our data demonstrate that Meg3 knockdown induced hepatic endothelial senescence which is associated with impaired glucose homeostasis and insulin signaling (Figs. 3 and 4), but the cause-effect relationship between them has not been established.

Here, we examined whether p53 deficiency in endothelium can attenuate cellular senescence in hepatic endothelium induced by Meg3 knockdown because p53 is a master regulator of cellular senescence and glucose homeostasis [85,86]. We took a genetic approach to reduce p53 expression in the vascular endothelium. We used conditional p53 floxed mice carrying tamoxifen-inducible Cre-recombinase under the regulation of the vascular endothelial cadherin promoter (p53 iECKO). The deletion of the p53 gene in endothelium was induced by tamoxifen injection, leading to 45% and 87% decrease in p53 expression in hepatic and skeletal muscle ECs, respectively, after 12 weeks (Fig. S8A). In

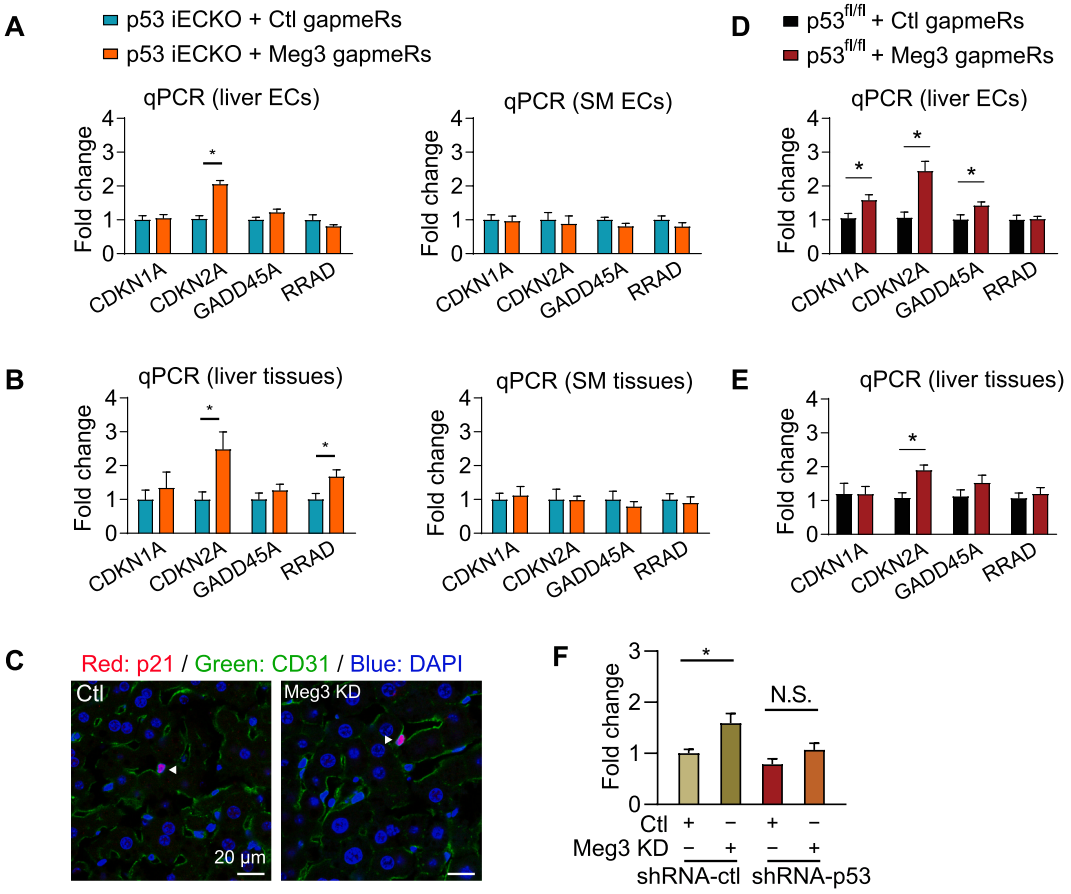

Fig. 5. Endothelial cell-specific p53 deletion attenuates Meg3 knockdown-induced cellular senescence of hepatic endothelium in obese mice. (A–C) p53 iECKO mice were fed a HFD. At Week 5 on HFD, mice were intravenously injected with control gapmeRs or Meg3 gapmeRs (knockdown) once a week and maintained on HFD for up to 12 weeks (n = 6–8 per group). (A) The expression of senescent markers (CDKN1A and CDKN2A) and p53 target genes (GADD45A and RRAD) were examined in the freshly isolated ECs by qPCR. (B) The expression of senescent markers (CDKN1A and CDKN2A) and p53 target genes (GADD45A and RRAD) were examined in livers and skeletal muscles (SM) tissues by qPCR. (C) Immunofluorescence staining of liver sections with anti-CD31 and anti-p21 antibodies. Arrowheads indicate double positive cells. (D–E) p53 floxed mice ($p53^{fl/fl}$) were fed a HFD. At Week 5 on HFD, mice were intravenously injected with control gapmeRs or Meg3 gapmeRs once a week and maintained on HFD for up to 12 weeks (n = 6–9 per group). (D) The expression of senescent markers (CDKN1A and CDKN2A) and p53 target genes (GADD45A and RRAD) were examined in the freshly isolated ECs by qPCR. (E) The expression of senescent markers (CDKN1A and CDKN2A) and p53 target genes (GADD45A and RRAD) were examined in livers by qPCR. (F) SA-β-gal staining of HUVECs transduced with control lentivirus (shRNA-ctl) or lentivirus expressing p53 shRNA (shRNA-p53), and transfected with control gapmeRs or Meg3 gapmeRs. The percentages of SA-β-gal positive cells were analyzed and fold changes were calculated relative to that in HUVECs transduced with shRNA-ctl and transfected with control gapmeRs. Data were from three independent experiments. For all panels, values are mean ± SEM; *, $P < 0.05$.

addition, the expression of p53 was reduced by 64% at protein levels in the freshly isolated liver ECs of p53 iECKO mice (Fig. S8B), which remarkably attenuated the expression of p21 at mRNA levels (Fig. S8C). In contrast, the expression of p53 was not changed in the livers and skeletal muscles (Fig. S8D). Systemic delivery of Meg3 gapmeRs reduced the expression of Meg3 in both ECs and liver and skeletal muscle tissues in either p53 iECKO (CadCreERT2:p53$^{fl/fl}$) mice (Fig. S8E) or p53$^{fl/fl}$ mice (data not shown).

We first examined the effects of Meg3 knockdown on cellular senescence of hepatic endothelium in p53 iECKO mice (Fig. 5A–C). In the ECs isolated from the livers, p53 deletion completely blocked the induction of *CDKN1A*, *GADD45A*, and *RRAD* in p53 iECKO mice injected with Meg3 gapmeRs as compared with that in mice injected with negative control gapmeRs (Fig. 5A). Interestingly, the expression of *CDKN2A* was still induced by Meg3 knockdown despite p53 deletion (Fig. 5A). In the liver tissue, *CDKN2A* and *RRAD* were induced by 2.5- and 1.7-fold, respectively (Fig. 5B). In the ECs isolated from the skeletal muscles, p53 deletion blocked the induction of *GADD45A* by Meg3 knockdown (Fig. 5A). The expression of all examined genes was not changed in the skeletal muscle (Fig. 5B). Of note, p21 expression was barely detectable by qPCR and immunostaining in both groups of mice (Fig. 5C, Fig. S8C), likely due to the deletion of p53.

We next examined the effects of Meg3 knockdown on cellular senescence of hepatic endothelium in p53$^{fl/fl}$ mice (Fig. 5D and E). Consistent with the data shown in Fig. 3, Meg3 knockdown causes cellular senescence in hepatic endothelium in obese p53$^{fl/fl}$ mice. Specifically, the expression of *CDKN1A*, *CDKN2A*, and *GADD45A* was elevated by 1.5-fold, 2.3-fold, and 1.4-fold, respectively, in the ECs isolated from the livers of obese p53$^{fl/fl}$ mice (Fig. 5D). The expression of *RRAD* was not changed in this experiment probably because p53$^{fl/fl}$ mice were less obese than those in Fig. 3.

We also examined the effects of p53 on Meg3 knockdown-induced EC senescence revealed by SA-β-gal activity staining. The expression of p53 was dramatically reduced by lentiviral p53 shRNA in HUVECs (data not shown). Meg3 knockdown led to a 1.6-fold increase in the number of SA-β-gal positive cells in HUVECs transduced with lentiviral control shRNAs, which was abolished in HUVECs transduced with lentiviral p53 shRNA (Fig. 5F).

Taken together, our data demonstrate p53 deletion in vascular endothelium can partially attenuate Meg3 knockdown-induced cellular senescence of hepatic vascular endothelium in diet-induced obese mice.

3.6. *Delaying the cellular senescence of hepatic endothelium by endothelial cell-specific p53 knockout attenuates the impaired glucose homeostasis and insulin signaling resulted from Meg3 knockdown*

We have shown that p53 deficiency in hepatic endothelium can attenuate Meg3 knockdown-induced cellular senescence in the hepatic

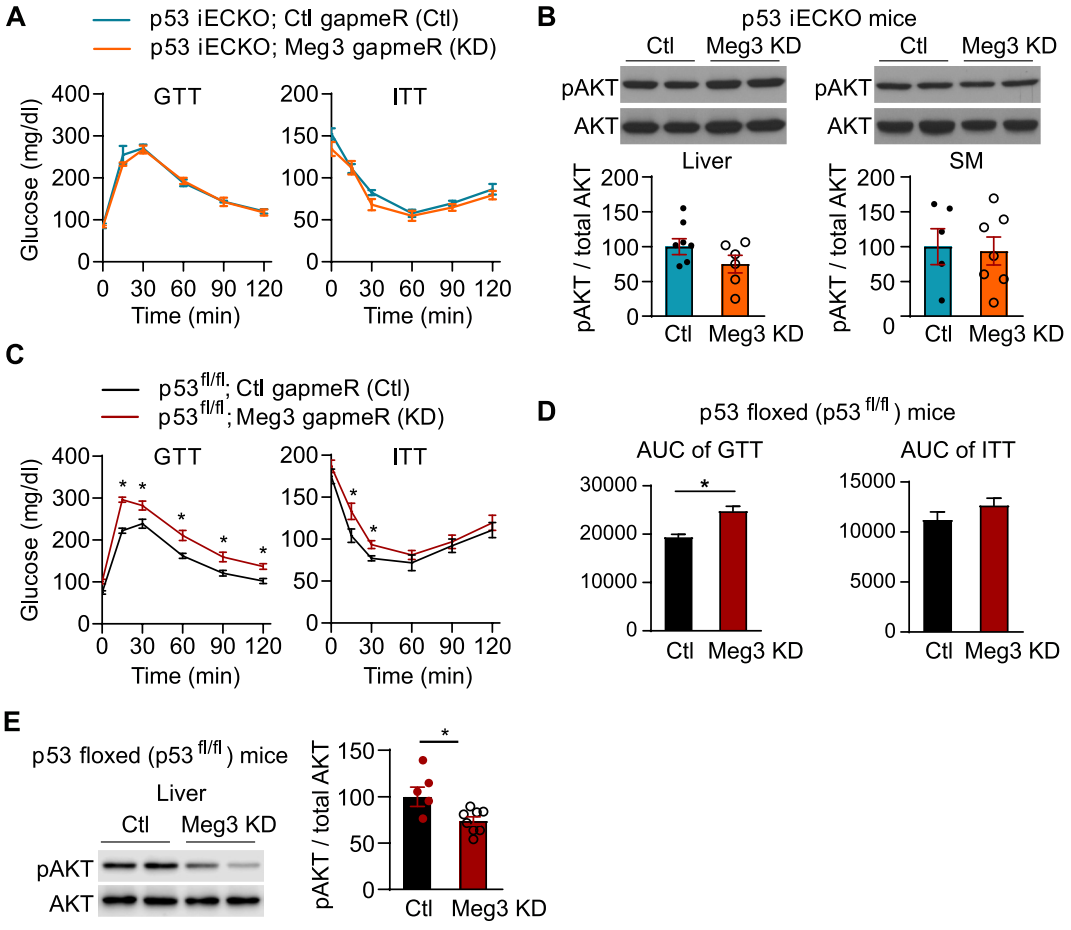

Fig. 6. Endothelial cell-specific p53 deletion attenuates Meg3 knockdown-impaired insulin signaling. (A–B) p53 iECKO mice were fed a HFD. At Week 5 on HFD, mice were intravenously injected with control gapmeRs or Meg3 gapmeRs (knockdown) once a week and maintained on HFD for up to 12weeks (n = 6–8 per group). (A) Glucose and insulin tolerance tests. (B) Total Akt and phosphorylated Akt at serine 473 were examined by western blot in the livers and skeletal muscles (SM) of overnight-fasted mice. The tissues were collected at 10 min after insulin injection (0.75 units/kg). (C–E) p53 floxed (p53$^{fl/fl}$) mice were fed a HFD. At Week 5 on HFD, mice were intravenously injected with control gapmeRs or Meg3 gapmeRs once a week and maintained on HFD for up to 12 weeks (n = 5–8 per group). (C) Glucose and insulin tolerance tests. (D) Areas under curves (AUC) for GTT and ITT. (E) Total Akt and phosphorylated Akt at serine 473 were examined by western blot in the livers of overnight-fasted mice. The livers were collected at 10 min after insulin injection (0.75 units/kg). For all panels, values are mean ± SEM; *, $P < 0.05$.

endothelium of obese mice. We next examined the role of cellular senescence of hepatic endothelium in glucose homeostasis and insulin signaling in obesity. Glucose tolerance test (GTT) and insulin tolerance test (ITT) revealed that Meg3 gapmeR-treated mice did not develop more severe glucose intolerance and insulin resistance after being fed a HFD for 10 weeks (Fig. 6A), when p53 expression was absent in hepatic endothelium. Next, we examined the effects of Meg3 knockdown on the phosphorylation of Akt at serine 473 in the livers and skeletal muscles of p53 iECKO mice (Fig. 6B). We did not examine the effect of Meg3 knockdown in eWAT in p53 iECKO mice, because Meg3 knockdown did not affect the phosphorylation of Akt in eWAT (Fig. 4E). The deletion of p53 in the vascular endothelium restored the phosphorylation of Akt in p53 iECKO mice injected with Meg3 gapmeRs to a level comparable to that observed in p53 iECKO mice injected with negative control gapmeRs in both liver and skeletal muscle (Fig. 6B). Consistent with the data in C57BL/6 mice (Fig. 4), Meg3 knockdown impaired glucose homeostasis and insulin signaling revealed by GTT, ITT, and western blot analysis of Akt phosphorylation at serine 473 in p53 floxed mice (Fig. 6C–E). Similarly, Meg3 knockdown also reduced the levels of phosphorylated IRβ by 25% (Fig. S9). These data demonstrate that the attenuation of cellular senescence of hepatic endothelium by deleting p53 expression can restore impaired glucose homeostasis and insulin signaling in obesity, suggesting that cellular senescence of hepatic endothelium drives obesity-induced insulin resistance and dysregulation of glucose homeostasis.

4. Discussion

In the present study, we examined the role of Meg3 in cellular senescence of HUVECs *in vitro*, and cellular senescence of hepatic endothelium, glucose homeostasis, and insulin signaling in diet-induced obesity. Our data demonstrate that: 1) Meg3 knockdown induces endothelial senescence *in vitro* and cellular senescence of hepatic endothelium in obese mice; 2) Meg3 knockdown impairs insulin signaling and glucose homeostasis in obesity; and 3) hepatic endothelial senescence promotes obesity-induced insulin resistance. Therefore, Meg3 expression in the vascular endothelium maintains glucose homeostasis and insulin signaling by protecting the hepatic endothelium against cellular senescence in obesity.

Cellular senescence is characterized by a number of hallmarks, including mitochondrial dysfunction, DNA damage, and increased expression of cyclin-dependent kinase inhibitors and SA-β-gal activity [1,4,87,88]. As we have shown that Meg3 knockdown inhibits cell proliferation, induces DNA damage [23], and others have shown that Meg3 knockdown decreases the length of telomeres in HUVECs [60], we wished to examine further markers of cellular senescence to firmly establish Meg3 as an important player in cellular senescence. We examined senescent hallmarks including SA-β-gal activity, mitochondrial dysfunction, and autophagy (Fig. 2). Our data strongly demonstrate that Meg3 prevents endothelial senescence *in vitro*. Importantly, we found Meg3 knockdown causes cellular senescence in hepatic vascular endothelium in obese mice (Fig. 3). In addition, the expression of Meg3 positively correlates with CDKN2A expression in human liver specimens (Fig. 3E). CDKN2A encodes p16, a commonly used marker of cellular senescence *in vivo* [3,77,78]. Meg3 expression was elevated by 1.6- and 1.9-fold, respectively, in NAFLD and NASH livers (Fig. 3E), suggesting that Meg3 induction is likely a compensatory mechanism in NAFLD and NASH livers in patients. Future studies will need to clarify this point. These data demonstrate that Meg3 is an important regulator of cellular senescence in vascular endothelium, which has not been previously reported.

While the precise mechanisms by which Meg3 knockdown induces cellular senescence are not fully elucidated, regulation of downstream p53 signaling and autophagy likely contribute. In support, we showed that p53 knockdown can block Meg3 knockdown-induced SA-β-gal activity (Fig. 5F), and the activation of autophagy by rapamycin can also attenuate Meg3 knockdown-induced SA-β-gal activity (Fig. 2H) in HUVECs. It is possible that Meg3 knockdown induces cellular senescence by impairing autophagy which results from the activation of p53 signaling upon Meg3 knockdown. It is also possible that Meg3 knockdown induces cellular senescence through cGAS-STING signaling, which can be activated in response to mitochondrial stress and DNA damage [89]. Indeed, Meg3 knockdown induces the expression of IFN-β and IRGM in hepatic endothelium in obese mice, and the expression of IFN-β and other interferon-stimulated genes in HUVECs (Fig. S6G), demonstrating that Meg3 knockdown activates type I interferon response *in vitro* and in hepatic endothelium in obese mice. These findings raise the possibility that cGAS-STING signaling contributes to cellular senescence induced by Meg3 knockdown *in vitro* and *in vivo*. Further studies are required to tease out the underlying molecular mechanism. One limitation to our data on Meg3's role in cellular senescence is that HUVECs were used for *in vitro* cell culture studies. Thus, our findings from HUVECs may not fully recapitulate the effects of Meg3 on cellular senescence of hepatic endothelium in obese mice. Specifically, the effects of Meg3 on additional features of cellular senescence such as impaired autophagy and mitochondrial structure and function were not examined in primary mouse liver sinusoidal ECs or in hepatic endothelium of mice in the present study. Future studies are warranted to provide further insights into this issue.

SQSTM1/p62 is a selective autophagy receptor that serves as a link between microtubule associated protein 1 light chain 3 (LC3) and ubiquitinated substrates of degradation [90]. During autophagy, p62, LC3-II (a lipidated form of LC3), and substrates become incorporated into autophagosomes and are degraded in autolysosomes (formed by the fusion of autophagosomes with lysosomes) [91]. Thus, the accumulation of p62 and LC3-II often correlates with impaired autophagy, while the reduction of p62 and LC3-II often associates with autophagy activation [91]. To exclude the possibility that the higher levels of p62 and LC3-II could activate autophagy, the expression of p62 and LC3-II needs to be examined in cells treated with Bafilomycin A1. It inhibits the degradation of p62 and LC3-II by blocking autophagosome-lysosome fusion and autolysosome acidification. When cells are treated with Bafilomycin A1, the persistent increase in p62 and LC3-II expression by the experimental condition indicates that autophagy is activated, while the normalization of p62 and LC3-II accumulation, respectively, between control and experimental conditions indicates that the accumulation of p62 and LC3-II results from impaired autophagy under basal condition. Our data in Fig. 2G demonstrate that Meg3 knockdown alters autophagic flux likely by impairing autophagy in HUVECs. Furthermore, we speculate that Meg3 knockdown leads to the accumulation of protein aggregates.

In this study, we examined the role of Meg3 in glucose homeostasis and insulin signaling in obesity, which has not been previously examined by other groups. GTT and ITT revealed that Meg3 knockdown impairs glucose homeostasis in obesity (Fig. 4B and C). Meg3 knockdown decreases insulin-stimulated Akt phosphorylation in livers and skeletal muscles (Fig. 4E), which is associated with an increase in fasting plasma insulin levels (Fig. 4D). In contrast, Meg3 knockdown had no effects on Akt phosphorylation in eWAT (Fig. 4E). The tissue-specific effects of other genes on Akt phosphorylation in major insulin target organs have been observed by other studies [92,93]. The tissue specific effects of Meg3 on insulin signaling could be due to the different microenvironment of different tissues. Chronic inflammation is a key driver of obesity-induced insulin resistance [82–84]. Meg3 knockdown had no effects on systemic inflammation (Fig. S6), suggesting Meg3 knockdown-induced insulin resistance is unlikely caused by its effects on systemic inflammation.

Obesity accelerates cellular senescence [17,94,95]. Elimination of p16-expressing senescent cells restored obesity-impaired neurogenesis and alleviated obesity-induced anxiety and metabolic dysfunction in obese mice [16,95]. However, the causal relationship between EC senescence and insulin resistance has not been examined in obesity. To answer the question, we employed a genetic approach to attenuate Meg3

knockdown-induced cellular senescence in obese mice. Specifically, we used *Cdh5CreERT2* Cre mice [24,25] to excise the floxed p53 exon in our studies. These mice express Cre driven by VE-cadherin promoter that is tamoxifen-inducible. This mouse line is most commonly used to excise sequences flanked by loxP sites in vascular endothelium [96,97], because it has more specific labelling of ECs than other mouse lines such as Tie2-Cre [98]. Furthermore, it is commonly used to excise loxP-sites flanking sequences in hepatic endothelium [97,99–101]. EC-specific p53 deletion attenuates DNA damage/cell senescence in obese mice [102]. Indeed, we found that EC-specific p53 knockout abrogates the induction of p21 and other p53 target genes such as *GADD45A* and *RRAD* upon Meg3 knockdown in hepatic vascular endothelium (Fig. 5A). Meg3 knockdown-induced p16 expression still persists in hepatic vascular endothelium with p53 deficiency, likely due to residual p53 expression in hepatic vascular endothelium. Importantly, we found that attenuation of hepatic EC senescence by EC-specific p53 knockout restores the impaired glucose homeostasis and hepatic insulin signaling, demonstrating that hepatic cell senescence promotes and attenuation of hepatic cell senescence ameliorates obesity-induced insulin resistance.

In conclusion, our data demonstrate that cellular senescence of hepatic endothelium promotes obesity-induced insulin resistance, which is tightly regulated by the expression of Meg3. Our data suggest that manipulation of Meg3 expression may represent a novel approach to managing obesity-associated hepatic endothelial senescence and insulin resistance.

Author contributions

X.C. and M.S.S. performed experiments and analysis. M.M., S.L.S, and M.C.Z. assisted with data analysis. X.S. and M.W.F. were involved in conceptualization. M.P.V. contributed to mitochondrial function assessment experiments, O.K. made intellectual contributions and helped to analyze and interpret the data. X.S. and X.C. wrote the paper. M. W.F. and M.C.Z. were involved in editing. X.S. and M.W.F. provided funds. All authors critically reviewed the manuscript.

Declaration of competing interest

The authors declare no competing financial or non-financial interests.

Acknowledgements

We thank Dr. Reinier Boon and Dr. Stefanie Dimmeler for providing the target sequence of human and mouse Meg3 gapmeRs, Dr. Jason C. Kovacic for providing *Cdh5CreERT2* Cre mice, Dr. Mi-Jeong Lee and Dr. Susan K. Fried for providing unidentified human white adipose tissues, and technologists Emily Barber and Mengna Xia at the Biomedical and Obesity Research Core of the Nebraska Center for Prevention of Obesity Diseases for assisting with mouse metabolic cage studies. Proteomics experiments in Fig. S7 were carried out by the Proteomics and Mass Spectrometry Core facility at Princeton University. EPR Spectroscopy data (Fig. 2C) was collected in the University of Nebraska's EPR Spectroscopy Core, which was established, in part, by a grant from the National Institute of General Medical Sciences of the National Institutes of Health (P30GM103335) awarded to the University of Nebraska's Redox Biology Center. This work was supported by the National Institutes of Health Funded COBRE grant 1P20GM104320 [X.S. through the Nebraska Center for the Prevention of Obesity-related Diseases through Dietary Molecules], the American Heart Association SDG#15SDG25400012 [to X.S.] and 18SFRN33900144 [to M.W.F.], and the National Institutes of Health Funded T32 grant 5T32GM107001-04 [to M.M.]. This work was also supported by the National Institutes of Health [HL150536 to X.S.; HL115141, HL134849, HL148207, HL148355, and HL153356 to M.W.F.; GM108975 and GM131701-01 to O.K.; P30GM103335 to the University of Nebraska's Redox Biology Center; and NIH Contract # HSN276201200017C to the Liver Tissue Cell Distribution System.]; and the Pilot and Feasibility Program [to X. S.] from Boston Nutrition Obesity Research Center funded by NIH grant P30DK046200. Funding for open access charge: National Institutes of Health.

Appendix A. Supplementary data

Supplementary data to this article can be found online at https://doi.org/10.1016/j.redox.2021.101863.

References

[1] A. Hernandez-Segura, J. Nehme, M. Demaria, Hallmarks of cellular senescence, Trends Cell Biol. 28 (6) (2018) 436–453.
[2] D. Munoz-Espin, M. Serrano, Cellular senescence: from physiology to pathology, Nat. Rev. Mol. Cell Biol. 15 (7) (2014) 482–496.
[3] N.E. Sharpless, C.J. Sherr, Forging a signature of in vivo senescence, Nat. Rev. Canc. 15 (7) (2015) 397–408.
[4] N. Herranz, J. Gil, Mechanisms and functions of cellular senescence, J. Clin. Invest. 128 (4) (2018) 1238–1246.
[5] A. Hernandez-Segura, et al., Unmasking transcriptional heterogeneity in senescent cells, Curr. Biol. : Cailiao Baohu 27 (17) (2017) 2652–2660.e4.
[6] A. Hernandez-Segura, R. Rubingh, M. Demaria, Identification of stable senescence-associated reference genes, Aging Cell 18 (2) (2019), e12911.
[7] P. Lecot, F. Alimirah, P.Y. Desprez, J. Campisi, C. Wiley, Context-dependent effects of cellular senescence in cancer development, Br. J. Canc. 114 (11) (2016) 1180–1184.
[8] M. Storer, et al., Senescence is a developmental mechanism that contributes to embryonic growth and patterning, Cell 155 (5) (2013) 1119–1130.
[9] D. Munoz-Espin, et al., Programmed cell senescence during mammalian embryonic development, Cell 155 (5) (2013) 1104–1118.
[10] M. Demaria, et al., An essential role for senescent cells in optimal wound healing through secretion of PDGF-AA, Dev. Cell 31 (6) (2014) 722–733.
[11] T. Feng, et al., CCN1-Induced cellular senescence promotes heart regeneration, Circulation 139 (21) (2019) 2495–2498.
[12] R. Sarig, et al., Transient p53-mediated regenerative senescence in the injured heart, Circulation 139 (21) (2019) 2491–2494.
[13] T.J. Bussian, et al., Clearance of senescent glial cells prevents tau-dependent pathology and cognitive decline, Nature 562 (7728) (2018) 578–582.
[14] D.J. Baker, et al., Naturally occurring p16(Ink4a)-positive cells shorten healthy lifespan, Nature 530 (7589) (2016) 184–189.
[15] P.J. Thompson, et al., Targeted elimination of senescent beta cells prevents type 1 diabetes, Cell Metabol. 29 (5) (2019) 1045–1060.e10.
[16] A.K. Palmer, et al., Targeting senescent cells alleviates obesity-induced metabolic dysfunction, Aging Cell 18 (3) (2019), e12950.
[17] D.G.A. Burton, R.G.A. Faragher, Obesity and type-2 diabetes as inducers of premature cellular senescence and ageing, Biogerontology 19 (6) (2018) 447–459.
[18] N. Jae, A.W. Heumuller, Y. Fouani, S. Dimmeler, Long non-coding RNAs in vascular biology and disease, Vasc. Pharmacol. 114 (2019) 13–22.
[19] V. Simion, S. Haemmig, M.W. Feinberg, LncRNAs in vascular biology and disease, Vasc. Pharmacol. 114 (2019) (2018) 145–156.
[20] S. Haemmig, et al., Long noncoding RNA SNHG12 integrates a DNA-PK-mediated DNA damage response and vascular senescence, Sci. Transl. Med. 12 (531) (2020) eaaw1868.
[21] T. Weirick, G. Militello, S. Uchida, Long non-coding RNAs in endothelial biology, Front. Physiol. 9 (2018) 522.
[22] A. Leung, V. Amaram, R. Natarajan, Linking diabetic vascular complications with LncRNAs, Vasc. Pharmacol. 114 (2019) (2018) 139–144.
[23] M.S. Shihabudeen Haider Ali, et al., LncRNA Meg3 protects endothelial function by regulating the DNA damage response, Nucleic Acids Res. 47 (3) (2019) 1505–1522.
[24] I. Sorensen, R.H. Adams, A. Gossler, DLL1-mediated Notch activation regulates endothelial identity in mouse fetal arteries, Blood 113 (22) (2009) 5680–5688.
[25] Y. Wang, et al., Ephrin-B2 controls VEGF-induced angiogenesis and lymphangiogenesis, Nature 465 (7297) (2010) 483–486.
[26] M. Konishi, et al., Endothelial insulin receptors differentially control insulin signaling kinetics in peripheral tissues and brain of mice, Proc. Natl. Acad. Sci. U. S. A. 114 (40) (2017) E8478–E8487.
[27] D.S. Ghorpade, et al., Hepatocyte-secreted DPP4 in obesity promotes adipose inflammation and insulin resistance, Nature 555 (7698) (2018) 673–677.
[28] D.J. Pedersen, et al., A major role of insulin in promoting obesity-associated adipose tissue inflammation, Mol Metab 4 (7) (2015) 507–518.
[29] Y.A. An, et al., Dysregulation of amyloid precursor protein impairs adipose tissue mitochondrial function and promotes obesity, Nat Metab 1 (12) (2019) 1243–1257.
[30] X. Li, Mechanisms by which adiponectin reverses high fat diet-induced insulin resistance in mice, Proc. Natl. Acad. Sci. U.S.A. 117 (51) (2020) 32584–32593.
[31] M. Kleinert, et al., Animal models of obesity and diabetes mellitus, Nat. Rev. Endocrinol. 14 (3) (2018) 140–162.

[32] R.J. Roth Flach, et al., Endothelial protein kinase MAP4K4 promotes vascular inflammation and atherosclerosis, Nat. Commun. 6 (2015) 8995.
[33] X. Sun, et al., MicroRNA-181b improves glucose homeostasis and insulin sensitivity by regulating endothelial function in white adipose tissue, Circ. Res. 118 (5) (2016) 810–821.
[34] Y.C. Lim, et al., Heterogeneity of endothelial cells from different organ sites in T-cell subset recruitment, Am. J. Pathol. 162 (5) (2003) 1591–1601.
[35] C.H. Chou, et al., Lysophosphatidic acid alters the expression profiles of angiogenic factors, cytokines, and chemokines in mouse liver sinusoidal endothelial cells, PloS One 10 (3) (2015), e0122060.
[36] J.R. van Beijnum, M. Rousch, K. Castermans, E. van der Linden, A.W. Griffioen, Isolation of endothelial cells from fresh tissues, Nat. Protoc. 3 (6) (2008) 1085–1091.
[37] C.S. Stein, et al., Mitoregulin: a lncRNA-encoded microprotein that supports mitochondrial supercomplexes and respiratory efficiency, Cell Rep. 23 (13) (2018) 3710–3720.e8.
[38] T. Issitt, et al., Neuropilin-1 controls endothelial homeostasis by regulating mitochondrial function and iron-dependent oxidative stress, iScience 11 (2019) 205–223.
[39] Y.M. Kim, et al., Redox regulation of mitochondrial fission protein drp1 by protein disulfide isomerase limits endothelial senescence, Cell Rep. 23 (12) (2018) 3565–3578.
[40] M.E. Kauffman, et al., MitoSOX-Based flow cytometry for detecting mitochondrial ROS, React Oxyg Species (Apex) 2 (5) (2016) 361–370.
[41] P. Mukhopadhyay, et al., Simultaneous detection of apoptosis and mitochondrial superoxide production in live cells by flow cytometry and confocal microscopy, Nat. Protoc. 2 (9) (2007) 2295–2301.
[42] A.J. Case, S. Li, U. Basu, J. Tian, M.C. Zimmerman, Mitochondrial-localized NADPH oxidase 4 is a source of superoxide in angiotensin II-stimulated neurons, Am. J. Physiol. Heart Circ. Physiol. 305 (1) (2013) H19–H28.
[43] A.J. Case, C.T. Roessner, J. Tian, M.C. Zimmerman, Mitochondrial superoxide signaling contributes to norepinephrine-mediated T-lymphocyte cytokine profiles, PloS One 11 (10) (2016), e0164609.
[44] B. Langmead, C. Trapnell, M. Pop, S.L. Salzberg, Ultrafast and memory-efficient alignment of short DNA sequences to the human genome, Genome Biol. 10 (3) (2009) R25.
[45] D. Kim, et al., TopHat2: accurate alignment of transcriptomes in the presence of insertions, deletions and gene fusions, Genome Biol. 14 (4) (2013) R36.
[46] B. Langmead, S.L. Salzberg, Fast gapped-read alignment with Bowtie 2, Nat. Methods 9 (4) (2012) 357–359.
[47] D.R. Zerbino, et al., Ensembl 2018, Nucleic Acids Res. 46 (D1) (2018) D754–D761.
[48] C. Trapnell, et al., Transcript assembly and quantification by RNA-Seq reveals unannotated transcripts and isoform switching during cell differentiation, Nat. Biotechnol. 28 (5) (2010) 511–515.
[49] C. Trapnell, et al., Differential analysis of gene regulation at transcript resolution with RNA-seq, Nat. Biotechnol. 31 (1) (2013) 46–53.
[50] M.D. Robinson, D.J. McCarthy, G.K. Smyth, edgeR: a Bioconductor package for differential expression analysis of digital gene expression data, Bioinformatics 26 (1) (2010) 139–140.
[51] R Core Development Team, R: A Language and Environment for Statistical Computing, R Foundation for Statistical Computing, Vienna, Austria), 2018.
[52] D.J. McCarthy, Y. Chen, G.K. Smyth, Differential expression analysis of multifactor RNA-Seq experiments with respect to biological variation, Nucleic Acids Res. 40 (10) (2012) 4288–4297.
[53] S. Anders, et al., Count-based differential expression analysis of RNA sequencing data using R and Bioconductor, Nat. Protoc. 8 (9) (2013) 1765–1786.
[54] K.J. Livak, T.D. Schmittgen, Analysis of relative gene expression data using real-time quantitative PCR and the 2(-Delta Delta C(T)) Method, Methods 25 (4) (2001) 402–408.
[55] O.M. Koval, et al., Loss of MCU prevents mitochondrial fusion in G1-S phase and blocks cell cycle progression and proliferation, Sci. Signal. 12 (579) (2019) eaav1439.
[56] R.A. Merrill, K.H. Flippo, S. Strack, Measuring mitochondrial shape with ImageJ. *Techniques to investigate mitochondrial Function in neurons*, in: S. Strack, Y. M. Usachev (Eds.), Springer New York, New York, NY), 2017, pp. 31–48.
[57] R.A. Boon, et al., Long noncoding RNA Meg3 controls endothelial cell aging and function: implications for regenerative angiogenesis, J. Am. Coll. Cardiol. 68 (23) (2016) 2589–2591.
[58] P. Fuschi, et al., Central role of the p53 pathway in the noncoding-RNA response to oxidative stress, Aging 9 (12) (2017) 2559–2586.
[59] P. Neumann, et al., The lncRNA GATA6-AS epigenetically regulates endothelial gene expression via interaction with LOXL2, Nat. Commun. 9 (1) (2018) 237.
[60] Y. Lan, et al., Long noncoding RNA MEG3 prevents vascular endothelial cell senescence by impairing miR-128-dependent Girdin downregulation, Am. J. Physiol. Cell Physiol. 316 (6) (2019) C830–C843.
[61] F. Debacq-Chainiaux, J.D. Erusalimsky, J. Campisi, O. Toussaint, Protocols to detect senescence-associated beta-galactosidase (SA-betagal) activity, a biomarker of senescent cells in culture and in vivo, Nat. Protoc. 4 (12) (2009) 1798–1806.
[62] B.G. Childs, et al., Senescent intimal foam cells are deleterious at all stages of atherosclerosis, Science 354 (6311) (2016) 472–477.
[63] J. Chapman, E. Fielder, J.F. Passos, Mitochondrial dysfunction and cell senescence: deciphering a complex relationship, FEBS Lett. 593 (13) (2019) 1566–1579.
[64] C.D. Wiley, et al., Mitochondrial dysfunction induces senescence with a distinct secretory phenotype, Cell Metabol. 23 (2) (2016) 303–314.
[65] D.V. Ziegler, C.D. Wiley, M.C. Velarde, Mitochondrial effectors of cellular senescence: beyond the free radical theory of aging, Aging Cell 14 (1) (2015) 1–7.
[66] P.V.S. Vasileiou, et al., Mitochondrial homeostasis and cellular senescence, Cells 8 (7) (2019) 686.
[67] A. Kopacz, et al., Keap1 governs ageing-induced protein aggregation in endothelial cells, Redox Biol 34 (2020), 101572.
[68] X. Sun, E.N. Harris, New aspects of hepatic endothelial cells in physiology and nonalcoholic fatty liver disease, Am. J. Physiol. Cell Physiol. 318 (6) (2020) C1200–C1213.
[69] S. Collins, T.L. Martin, R.S. Surwit, J. Robidoux, Genetic vulnerability to diet-induced obesity in the C57BL/6J mouse: physiological and molecular characteristics, Physiol. Behav. 81 (2) (2004) 243–248.
[70] C.Y. Wang, J.K. Liao, A mouse model of diet-induced obesity and insulin resistance, Methods Mol. Biol. 821 (2012) 421–433.
[71] L.M. Williams, et al., The development of diet-induced obesity and glucose intolerance in C57BL/6 mice on a high-fat diet consists of distinct phases, PloS One 9 (8) (2014), e106159.
[72] R.S. Surwit, C.M. Kuhn, C. Cochrane, J.A. McCubbin, M.N. Feinglos, Diet-induced type II diabetes in C57BL/6J mice, Diabetes 37 (9) (1988) 1163–1167.
[73] M.S. Winzell, B. Ahren, The high-fat diet-fed mouse: a model for studying mechanisms and treatment of impaired glucose tolerance and type 2 diabetes, Diabetes 53 (3) (2004) S215–S219.
[74] E. Leucci, et al., Melanoma addiction to the long non-coding RNA SAMMSON, Nature 531 (7595) (2016) 518–522.
[75] L. Natarelli, et al., miR-103 promotes endothelial maladaptation by targeting lncWDR59, Nat. Commun. 9 (1) (2018) 2645.
[76] V. Krizhanovsky, et al., Senescence of activated stellate cells limits liver fibrosis, Cell 134 (4) (2008) 657–667.
[77] J.Y. Liu, et al., Cells exhibiting strong p16 (INK4a) promoter activation in vivo display features of senescence, Proc. Natl. Acad. Sci. U. S. A. 116 (7) (2019) 2603–2611.
[78] M. Ogrodnik, et al., Cellular senescence drives age-dependent hepatic steatosis, Nat. Commun. 8 (2017) 15691.
[79] T. Minamino, et al., A crucial role for adipose tissue p53 in the regulation of insulin resistance, Nat. Med. 15 (9) (2009) 1082–1087.
[80] S.V. Brodsky, et al., Prevention and reversal of premature endothelial cell senescence and vasculopathy in obesity-induced diabetes by ebselen, Circ. Res. 94 (3) (2004) 377–384.
[81] C.Y. Wang, et al., Obesity increases vascular senescence and susceptibility to ischemic injury through chronic activation of Akt and mTOR, Sci. Signal. 2 (62) (2009) ra11.
[82] G.S. Hotamisligil, Inflammation, metaflammation and immunometabolic disorders, Nature 542 (7640) (2017) 177–185.
[83] Y.S. Lee, J. Wollam, J.M. Olefsky, An integrated view of immunometabolism, Cell 172 (1–2) (2018) 22–40.
[84] M.C. Petersen, G.I. Shulman, Mechanisms of insulin action and insulin resistance, Physiol. Rev. 98 (4) (2018) 2133–2223.
[85] E.R. Kastenhuber, S.W. Lowe, Putting p53 in context, Cell 170 (6) (2017) 1062–1078.
[86] F. Kruiswijk, C.F. Labuschagne, K.H. Vousden, p53 in survival, death and metabolic health: a lifeguard with a licence to kill, Nat. Rev. Mol. Cell Biol. 16 (7) (2015) 393–405.
[87] D.J. Baker, R.C. Petersen, Cellular senescence in brain aging and neurodegenerative diseases: evidence and perspectives, J. Clin. Invest. 128 (4) (2018) 1208–1216.
[88] V. Gorgoulis, et al., Cellular senescence: defining a path forward, Cell 179 (4) (2019) 813–827.
[89] T. Li, Z.J. Chen, The cGAS-cGAMP-STING pathway connects DNA damage to inflammation, senescence, and cancer, J. Exp. Med. 215 (5) (2018) 1287–1299.
[90] V. Kirkin, V.V. Rogov, A diversity of selective autophagy receptors determines the specificity of the autophagy pathway, Mol. Cell 76 (2) (2019) 268–285.
[91] D.J. Klionsky, et al., Guidelines for the use and interpretation of assays for monitoring autophagy (3rd edition), Autophagy 12 (1) (2016) 1–222.
[92] J. Chung, et al., HSP72 protects against obesity-induced insulin resistance, Proc. Natl. Acad. Sci. U. S. A. 105 (5) (2008) 1739–1744.
[93] E.P. Crowe, et al., Changes in the transcriptome of human astrocytes accompanying oxidative stress-induced senescence, Front. Aging Neurosci. 8 (2016) 208.
[94] M. Tencerova, et al., Obesity-associated hypermetabolism and accelerated senescence of bone marrow stromal stem cells suggest a potential mechanism for bone fragility, Cell Rep. 27 (7) (2019) 2050–2062.e6.
[95] M. Ogrodnik, et al., Obesity-induced cellular senescence drives anxiety and impairs neurogenesis, Cell Metabol. 29 (5) (2019) 1233.
[96] S. Payne, S. De Val, A. Neal, Endothelial-specific Cre mouse models, Arterioscler. Thromb. Vasc. Biol. 38 (11) (2018) 2550–2561.
[97] J. Poisson, et al., Liver sinusoidal endothelial cells: physiology and role in liver diseases, J. Hepatol. 66 (1) (2017) 212–227.
[98] Y. Tang, A. Harrington, X. Yang, R.E. Friesel, L. Liaw, The contribution of the Tie2 + lineage to primitive and definitive hematopoietic cells, Genesis 48 (9) (2010) 563–567.
[99] A. Hammoutene, et al., A defect in endothelial autophagy occurs in patients with non-alcoholic steatohepatitis and promotes inflammation and fibrosis, J. Hepatol. 72 (3) (2020) 528–538.

[100] M. Ruart, et al., Impaired endothelial autophagy promotes liver fibrosis by aggravating the oxidative stress response during acute liver injury, J. Hepatol. 70 (3) (2019) 458–469.

[101] B.S. Ding, et al., Inductive angiocrine signals from sinusoidal endothelium are required for liver regeneration, Nature 468 (7321) (2010) 310–315.

[102] M. Yokoyama, et al., Inhibition of endothelial p53 improves metabolic abnormalities related to dietary obesity, Cell Rep. 7 (5) (2014) 1691–1703.